# Delft University of Technology

## Mechanical Control of a Single Nuclear Spin

Maity, Smarak; Pingault, Benjamin; Joe, Graham; Chalupnik, Michelle; Assumpção, Daniel; Cornell, Eliza; Shao, Linbo; Lončar, Marko

**Important note**
To cite this publication, please use the final published version (if applicable).
Please check the document version above.

# Mechanical Control of a Single Nuclear Spin

Smarak Maity,[1,*] Benjamin Pingault,[1,2,3,*] Graham Joe,[1] Michelle Chalupnik,[4]
Daniel Assumpção[ORCID],[1] Eliza Cornell,[1] Linbo Shao[ORCID],[1] and Marko Lončar[ORCID][1,†]

[1]*John A. Paulson School of Engineering and Applied Sciences, Harvard University,
Cambridge, Massachusetts 02138, USA*
[2]*QuTech, Delft University of Technology, 2600 GA Delft, The Netherlands*
[3]*Kavli Institute of Nanoscience Delft, Delft University of Technology, 2600 GA Delft, The Netherlands*
[4]*Department of Physics, Harvard University, Cambridge, Massachusetts 02138, USA*

Nuclear spins interact weakly with their environment and therefore exhibit long coherence times. This has led to their use as memory qubits in quantum information platforms, where they are controlled via electromagnetic waves. Scaling up such platforms comes with challenges in terms of power efficiency, as well as cross-talk between devices. Here, we demonstrate coherent control of a single nuclear spin using surface acoustic waves. We use mechanically driven Ramsey and spin-echo sequences to show that the nuclear spin retains its excellent coherence properties. We estimate that this approach requires 2–3 orders of magnitude less power than more conventional control methods. Furthermore, this technique is scalable because of the possibility of guiding acoustic waves and reduced cross-talk between different acoustic channels. This work demonstrates the use of mechanical waves for complex quantum control sequences, offers an advantageous alternative to the standard electromagnetic control of nuclear spins, and opens prospects for incorporating nuclear spins in mechanically interfaced hybrid quantum architectures.

## I. INTRODUCTION

Nuclear spins couple weakly to their environment and thus display the longest coherence times among all solid-state systems [1–3], making them desirable quantum memories. They have been incorporated into various quantum information protocols such as error correction [4], quantum teleportation [5], entanglement distillation [6], and multiqubit entanglement, between both local [2] and distant [7] qubits. Two main approaches have been developed to control nuclear spins: direct radio frequency driving [1,2,8–10] and indirect microwave driving via the hyperfine coupling to a neighboring electronic spin [4,11,12]. An alternative approach using all-electrical control has been demonstrated, by using ensembles of nuclear spins [13], by relying on the presence of a quadrupolar interaction [14], or by using a second-order hyperfine Stark effect in single molecules [15]. Mechanical interfacing of nuclear spins would be highly desirable for

hybrid quantum architectures, owing to the ability of mechanical vibrations to couple to diverse quantum systems [16–18]. So far, only signatures of coupling between mechanical vibrations and nuclear spin ensembles via the quadrupolar interaction have been shown [19,20], with a recent proposal to extend this technique to single nuclear spins [21]. However, mechanical control of single nuclear spins has not yet been demonstrated, and it is unclear whether the coherence of the nuclear spins would be negatively impacted. Here, we demonstrate the control of a single nuclear spin using mechanical vibrations, with a technique that is compatible with any nuclear spin. We demonstrate effective Rabi frequencies of about 10 kHz, which is comparable to other techniques [1,2,9,10], and we confirm that the nuclear spin retains its excellent coherence properties. This approach has several advantages for scalability: Mechanical waves are generated using surface acoustic devices, which are relatively easy to fabricate. Mechanical waves cannot propagate in free space, which can be leveraged to limit cross-talk, and they can be efficiently guided on chip using acoustic waveguides [22–26]. Finally, this approach requires about 2–3 orders of magnitude less power compared to other approaches [1,2,9,13,14,27], thereby reducing heating, which is a concern for many low-temperature experiments [2,12,28]. Our results demonstrate the suitability of mechanical vibrations for implementing complex quantum control sequences. Such mechanical

---
[*]These authors contributed equally to this work.
[†]loncar@seas.harvard.edu

control also opens the way to integrating long-lived nuclear spins in hybrid quantum architectures in which mechanics is used as a quantum bus linking different types of qubits [16–18].

## II. RESULTS

In our experiments, the interaction between the nuclear spin and mechanical vibrations is mediated by a single, negatively charged, silicon-vacancy center (SiV). The mechanical vibrations are surface acoustic waves (SAWs), which have natural two-dimensional confinement, can be guided on chip and are easily generated by electrical excitation of interdigital transducers (IDTs) [29]. We pattern aluminium IDTs on top of a layer of piezoelectric aluminium nitride deposited on the surface of a single-crystal diamond. The diamond sample is ultrapure (nitrogen concentration less than 5 ppb) and has a natural abundance of the $^{13}$C isotope (1.1%). The diamond is implanted with $^{28}$Si$^+$ ions and annealed to form SiV centers, which can be optically addressed individually. The SiVs are located within the strain field of the SAW, which extends about a wavelength (about 3 $\mu$m) below the surface of the diamond [Fig. 1(a)]. The sample is cooled to below 200 mK in a dilution refrigerator to increase the lifetime of the SiV electron spin ($S = 1/2$) [30]. An external magnetic field of 0.13 T at an angle of 90° with respect to the SiV axis lifts the spin degeneracy and introduces a splitting of $f_{\downarrow\uparrow} = 3.42$ GHz between the $|\downarrow\rangle$ and $|\uparrow\rangle$ spin states [Fig. 1(b)]. The field angle of 90° is chosen to maximize the strain susceptibility of the SiV spin [31]. The optical transition labeled $\downarrow\downarrow'$ can be excited resonantly by laser pulses to initialize the SiV in $|\uparrow\rangle$ via optical pumping, while the $\downarrow\uparrow$ transition can be driven acoustically to coherently transfer population between $|\downarrow\rangle$ and $|\uparrow\rangle$ [29].

The mechanical coupling to the $^{13}$C nuclear spin ($S = 1/2$) relies on the simultaneous coupling of a SiV electronic spin to acoustic waves and to the nuclear spin. An individual $^{13}$C nuclear spin couples to a SiV spin via the hyperfine interaction Hamiltonian

$$\mathcal{H} = 2\pi\hbar S_z^{\text{SiV}}(A_\| S_z^{\text{nuc}} + A_\perp S_x^{\text{nuc}}),$$

where $S_i = \sigma_i/2$ are the spin operators, with $\sigma_i$ being the Pauli matrices for $i \in \{x, y, z\}$ ("SiV" and "nuc" indicate SiV and nuclear spins, respectively), and $A_\|$ and $A_\perp$ are the parallel and perpendicular components of the hyperfine coupling. This coupling causes the nuclear spin to precess about slightly different axes depending on the state of the SiV spin. This can be utilized to control the nuclear spin state [4,27,32] with the basic sequence depicted in Fig. 1(c). After the SiV spin is initialized in $|\uparrow\rangle$, a series of periodically timed acoustic pulses (with interpulse delay $\tau$) flip its state repeatedly, causing the nuclear spin to alternate between two different precession axes. If the acoustic pulses are synchronized with the precession of the nuclear spin, such that [4,12]
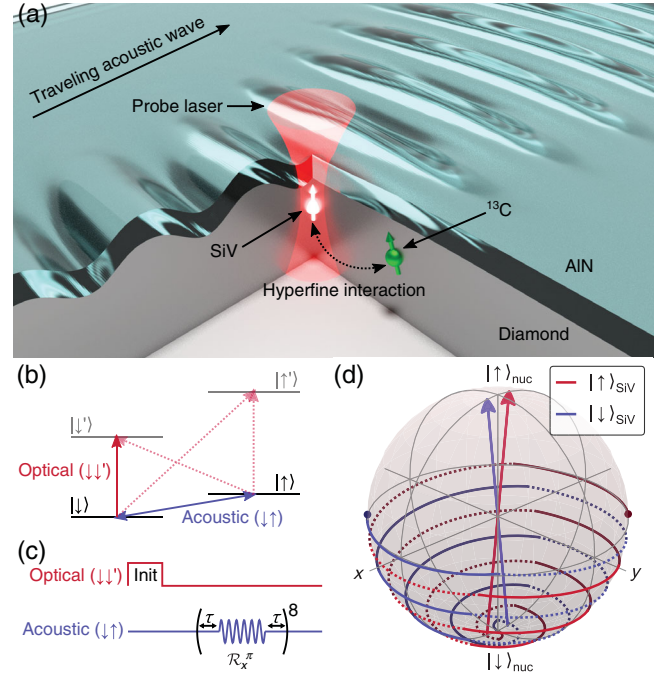


FIG. 1.   Principle behind mechanical coupling to nuclear spins. (a) Schematic of the system. Surface acoustic waves (SAWs) generated in the AlN layer, and extending into diamond, are used to control the $^{13}$C nuclear spin via its hyperfine coupling to the silicon vacancy (SiV) electron spin, which can be initialized and read out optically. (b) Simplified electronic structure of the SiV in the presence of an external magnetic field. The red arrows (both dashed and solid) indicate optical transitions around 737 nm. The solid red arrow corresponds to the transition ($\downarrow\downarrow'$) used for optical pumping to initialize the SiV state in $|\uparrow\rangle$. The blue arrow corresponds to the 3.42-GHz spin-flipping transition $\downarrow\uparrow$ that can be driven acoustically. (c) Schematic of a sequence that induces conditional precession of the nuclear spin. The optical part corresponds to the optical initialization of the SiV spin into $|\uparrow\rangle$. The SiV spin can be initialized in $|\downarrow\rangle$ by exciting the $\uparrow\uparrow'$ transition. The acoustic part corresponds to a series of eight, periodically timed, acoustic $\pi$ pulses around the $X$ axis of the Bloch sphere ($\mathcal{R}_x^\pi$). (d) Simulation of the evolution of the nuclear spin on the Bloch sphere for the sequence described in diagram (c). The red (blue) arrow corresponds to the nuclear spin precession axis when the SiV is in $|\uparrow\rangle$ ($|\downarrow\rangle$). The nuclear spin starts in $|\downarrow\rangle_{\text{nuc}}$ and follows the red (blue) trajectory when the SiV is initially in $|\uparrow\rangle$ ($|\downarrow\rangle$). Spin flips of the SiV are indicated by transitions between solid and dashed trajectories. The red (blue) dot indicates the final state of the nuclear spin for the SiV initially in state $|\uparrow\rangle$ ($|\downarrow\rangle$). The hyperfine coupling parameters used are $\{A_\| = 0.11$ MHz, $A_\perp = 0.33$ MHz$\}$, and the interpulse time is $\tau = 0.169$ $\mu$s.

$$\tau \approx \frac{2k+1}{4f_L}\left[1 - \frac{A_\perp^2}{8f_L^2}\right],$$

for integer values of $k$, where $f_L$ is the nuclear Larmor frequency, the nuclear spin rotates on the Bloch sphere by an angle $\phi$, around an effective axis **n**. The angle $\phi$ is determined

by $\tau$ and the number of pulses $N$, while the effective rotation axis $\mathbf{n}_\downarrow$ or $\mathbf{n}_\uparrow$ depends on $\tau$ and the initial state ($|\downarrow\rangle$ or $|\uparrow\rangle$) of the SiV spin. Figure 1(d) depicts the effect of the sequence for the initial states $|\downarrow\rangle_{\mathrm{SiV}}|\downarrow\rangle_{\mathrm{nuc}}$ and $|\uparrow\rangle_{\mathrm{SiV}}|\downarrow\rangle_{\mathrm{nuc}}$, where the final state of the nuclear spin depends on the initial state of the SiV spin. This is a conditional rotation gate, denoted by $\mathcal{R}^\phi_{\mathbf{n}_\downarrow,\mathbf{n}_\uparrow}$, that entangles the SiV and nuclear spins, and it is the building block of all the nuclear spin control sequences performed in this work.

We identify a target $^{13}$C spin by performing nuclear spin resonance spectroscopy using the SiV [4,32]. The SiV spin is initialized in $|\uparrow\rangle$, after which an acoustic pulse performs a $\pi/2$ rotation of the spin to bring it into the superposition state $(|\uparrow\rangle + |\downarrow\rangle)/\sqrt{2}$. A series of acoustic $\pi$ pulses then perform an XY8 sequence [33], whereby the SiV spin is flipped repeatedly around two different axes ($X$, $Y$) on the Bloch sphere, depending on the phase (0 or $\pi/2$) of each pulse [Fig. 2(a)]. A final acoustic $\pi/2$ pulse is then applied to the SiV spin before its state is read out by optical excitation of the $\downarrow\downarrow'$ transition and collection of the resulting fluorescence. This pulse sequence increases the coherence time of the SiV spin by decoupling it from magnetic field noise [34] while allowing its selective coupling to individual $^{13}$C nuclear spins. Figure 2(b) shows the measurement of the SiV population in $|\downarrow\rangle$ after an XY8 sequence as the interpulse time $\tau$ is varied. For values of $\tau$ corresponding to resonance with a particular $^{13}$C spin, the SiV spin state coherently evolves in conjunction with the nuclear spin. This appears as periodic sharp dips. The most prominent dips in Fig. 2(b) can be ascribed to a single nuclear spin, and their positions and depths can be modeled to extract the hyperfine coupling parameters $\{A_\parallel = 0.11 \text{ MHz}, A_\perp = 0.33 \text{ MHz}\}$ [34].

Having identified the target nuclear spin, we proceed to initialize it. The sequence for nuclear spin initialization is shown in Fig. 3(a). It consists of $\pi/2$ rotations of the SiV spin and conditional rotations of the nuclear spin implemented as XY8 sequences on the SiV spin [4,27,32]. We simulate the state of the nuclear spin at the end of the initialization sequence for values of the interpulse delay $\tau$ in the vicinity of the $\tau = 1.578$ $\mu$s resonance, as shown in Fig. 3(b). For $\tau = 1.569$ $\mu$s, if the SiV is set to $|\uparrow\rangle_{\mathrm{SiV}}$ ($|\downarrow\rangle_{\mathrm{SiV}}$) at the beginning of the sequence, the nuclear spin is initialized in $|\downarrow\rangle_{\mathrm{nuc}}$ ($|\uparrow\rangle_{\mathrm{nuc}}$) at the end of it. The nuclear spin readout sequence corresponds to the same sequence in reverse, and it transfers the nuclear spin onto the SiV spin. The experimental results for the full sequence for various values of $\tau$ are shown as dots in Fig. 3(c), with simulations shown as solid curves. For $\tau = 1.569$ $\mu$s, the final state of the SiV depends on the state in which the nuclear spin was initialized. The experimental data agree with the expected results from the simulation, thus confirming the successful initialization and readout of the nuclear spin. The parasitic partial addressing of other $^{13}$C nuclear spins with similar hyperfine couplings to the SiV limits the fidelity of the
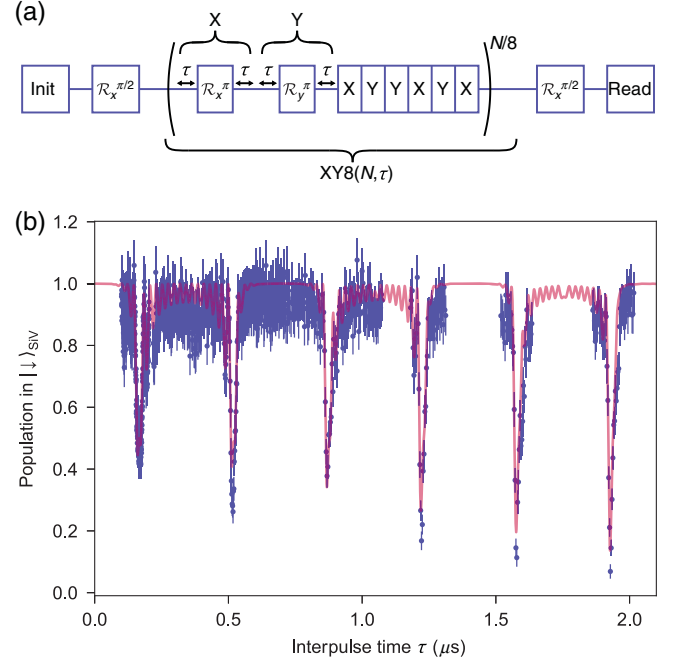


FIG. 2. Nuclear spin resonance spectroscopy using an XY8 decoupling sequence on the SiV spin. (a) Schematic of the XY8 sequence. Here, $\mathcal{R}^\theta_{\mathbf{x}}$ ($\mathcal{R}^\theta_{\mathbf{y}}$) represents a pulse that rotates the SiV spin by an angle $\theta$ around the $X$ ($Y$) axis of the Bloch sphere. Note that "init" and "read" represent optical initialization and readout, respectively, and $N$ is the total number of $\pi$ pulses. (b) Measurement of the final SiV spin population in $|\downarrow\rangle$ for an XY8 sequence with $N = 16$ pulses, as a function of the interpulse time $\tau$. The blue dots correspond to the experimental data. The error bars represent the standard deviation of the measured SiV spin population, from photon counting statistics [34]. A fit (red curve) to the data yields the hyperfine coupling parameters $\{A_\parallel = 0.11 \text{ MHz}, A_\perp = 0.33 \text{ MHz}\}$ for the target nuclear spin [34].

initialization and readout sequences to 0.91 [34]. The experimentally measured fidelities are $0.85 \pm 0.03$ and $0.91 \pm 0.02$ for initialization into the $|\downarrow\rangle_{\mathrm{nuc}}$ and $|\uparrow\rangle_{\mathrm{nuc}}$ states, respectively, with readout fidelities equal to the initialization fidelities. Although a similar initialization sequence could be constructed with $\tau = 1.586$ $\mu$s, its fidelity is inferior, as seen in Fig. 3(c), because of parasitic partial addressing of other nuclear spins. The fidelity can be improved by operating at longer interpulse delay times to better resolve individual nuclear spin resonances.

If the interpulse delay is $\tau' = 1.578$ $\mu$s, the XY8 sequence rotates the nuclear spin around the $X$ axis of the Bloch sphere by an angle dependent on the number of pulses $N'$ in the sequence. By inserting such an XY8 sequence between the nuclear spin initialization and readout sequences [Fig. 3(d)], and varying $N'$, we perform coherent rotations of the nuclear spin, as demonstrated by the observation of Rabi oscillations shown in Fig. 3(e). We note that $N' = 8$ corresponds to a $\pi/2$ rotation of the nuclear spin. Based on the duration of the sequence required for a $2\pi$ rotation, we estimate an effective Rabi
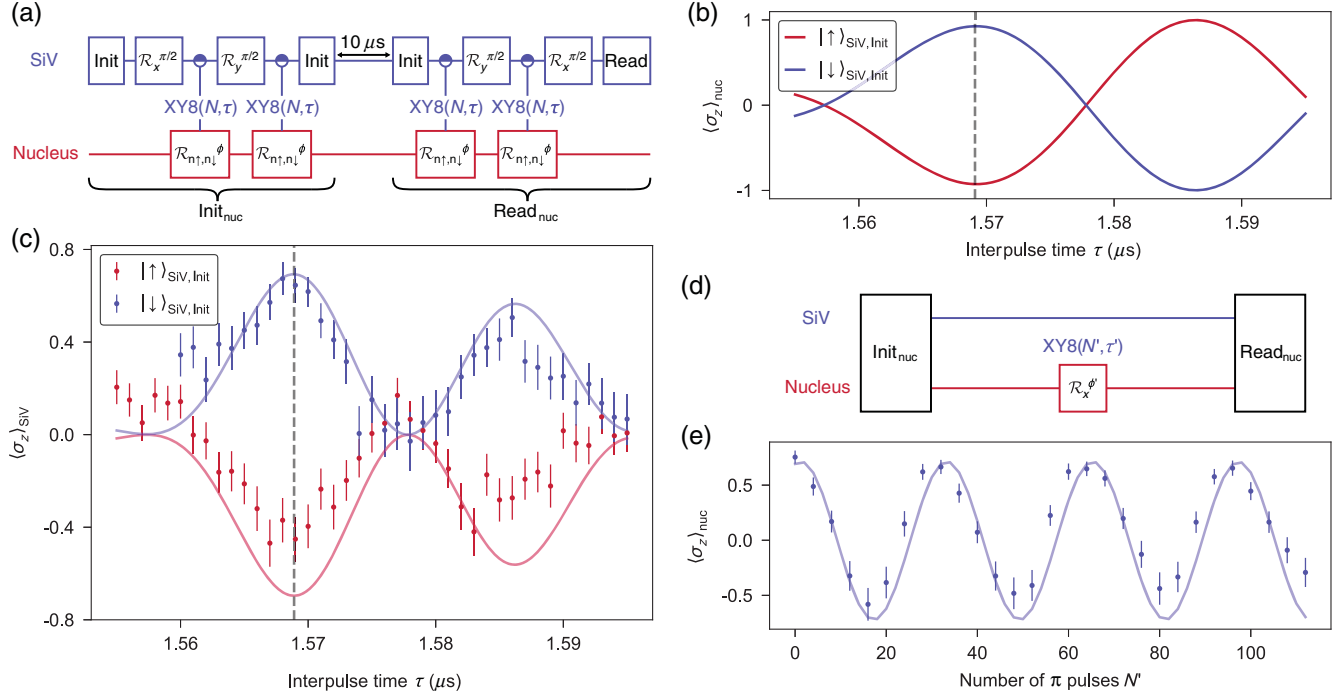
FIG. 3. Mechanical control of a single $^{13}$C nuclear spin. (a) Sequences for mechanically driven nuclear spin initialization (init$_{\text{nuc}}$) and readout (read$_{\text{nuc}}$). These are based on entangling conditional rotations of the form $\mathcal{R}_{\mathbf{n}\downarrow,\mathbf{n}\uparrow}^{\phi}$ implemented as acoustic XY8 sequences on the SiV spin. (b) Simulation of the state of the nuclear spin after the nuclear initialization sequence for $N = 16$ pulses as a function of the interpulse time $\tau$. The red (blue) curve corresponds to a sequence at the beginning of which the SiV spin is in the state $|\uparrow\rangle$ ($|\downarrow\rangle$). The dashed gray line indicates the value of $\tau = 1.569 \ \mu s$ later used for nuclear spin initialization. (c) Measurement (dots) and simulation (solid curves) of the final SiV spin projection after the nuclear initialization and readout sequences, as a function of $\tau$, for different initial states of the SiV spin. The measured optimal value of $\tau \approx 1.569 \ \mu s$ (dashed gray line) agrees with simulations. The simulation includes the effect of a second nonresonant nuclear spin with weaker hyperfine couplings, which accounts for the reduction in fidelity [34]. (d) Sequence for coherent control of the nuclear spin. After nuclear initialization with $\tau = 1.569 \ \mu s$, an XY8 sequence with $\tau' = 1.578 \ \mu s$ rotates the nuclear spin around the $X$ axis of the Bloch sphere with an angle $\phi'$ depending on the number of $\pi$ pulses ($N'$). (e) Mechanically driven Rabi oscillations of the nuclear spin, corresponding to the sequence in diagram (d). The dots represent measured values, while the solid curve corresponds to a simulation using previously determined hyperfine coupling parameters. The error bars in diagrams (c) and (e) represent the standard deviations of the measured quantities.

frequency $\Omega^{\text{nuc}} = 2\pi \times 9.8$ kHz [34]. For these sequences, the peak input microwave power is 0.63 mW, with the peak on-chip acoustic power estimated to be no higher than 14 $\mu$W. The average powers are lower by about 2 orders of magnitude because of the pulsed nature of the control sequence [34].

We then evaluate the coherence of the nuclear spin under mechanical control using Ramsey interferometry. We perform two $\pi/2$ rotations of the nuclear spin separated by a variable delay, whereby the nuclear spin is brought into a superposition state that precesses freely before being read out [Fig. 4(a)]. Immediately after the first $\pi/2$ rotation of the nuclear spin, the SiV is initialized in either $|\uparrow\rangle$ (red dots) or $|\downarrow\rangle$ (blue dots), which causes the nuclear spin to process at a rate that depends on the state of the SiV spin, as shown in Fig. 4(b), with precession frequencies $f_{\uparrow,\downarrow}^{\text{Ramsey}} = \sqrt{(f_L \pm A_\parallel/2)^2 + (A_\perp/2)^2}$. This difference in precession frequencies confirms that we address a single

nuclear spin. We repeat the measurement for longer free precession times for a single orientation of the SiV spin, as displayed in Fig. 4(c). The amplitude of the Ramsey oscillations does not decrease up to precession times of 2 ms, indicating that the nuclear spin retains its coherence above this timescale, $T_2^* \gg 2$ ms. Next, we perform a spin-echo sequence by inserting a nuclear $\pi$ rotation between the two $\pi/2$ rotations, as illustrated in Fig. 4(d). The $\pi$ rotation cancels the impact of any dephasing mechanism that is slower than the free precession timescale. The nuclear spin state at the end of the sequence is plotted as a function of the total precession time in Fig. 4(e) and shows no sign of decay, indicating $T_2^{\text{echo}} \gg 10$ ms. Because of the limited photon collection efficiency of our system, measurements for longer precession times are impractical, considering the experimental times required. Nevertheless, our measurements confirm that the $^{13}$C nuclear spin retains long coherence times [2,27] under mechanical control.
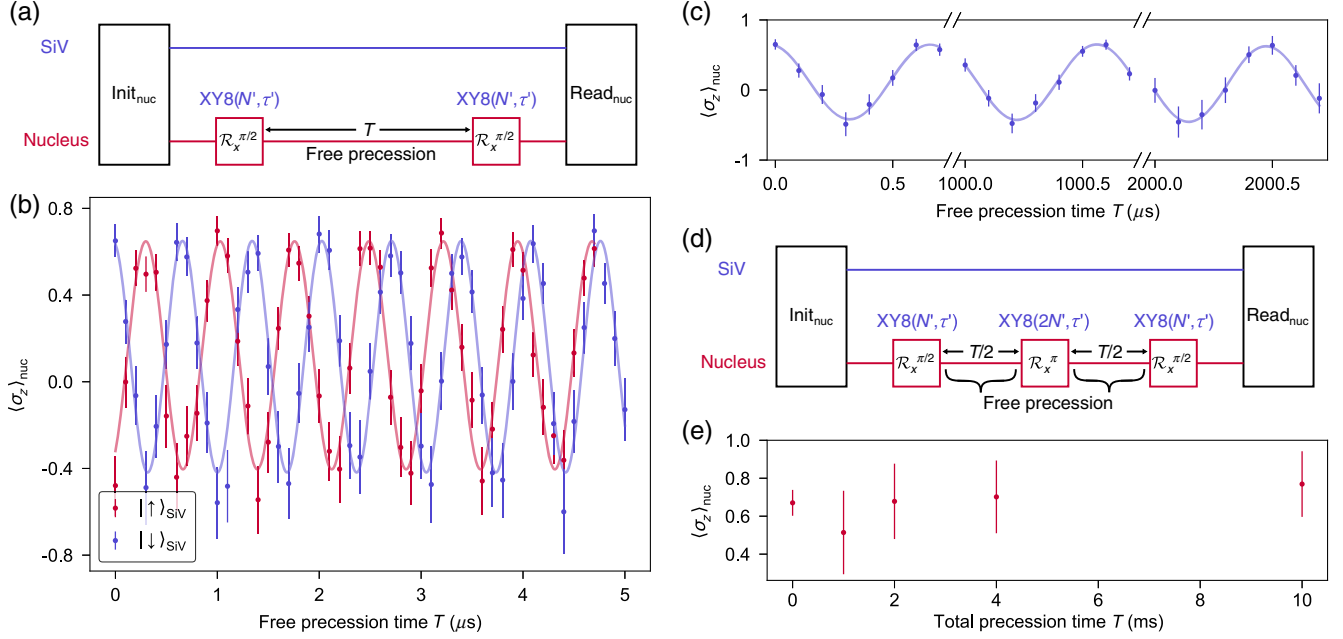
FIG. 4. Mechanically driven Ramsey interferometry and spin echo of the $^{13}$C nuclear spin. (a) Sequence for Ramsey interferometry. Two $\phi' = \pi/2$ rotations of the nuclear spin, corresponding to XY8 sequences with $N' = 8$ and $\tau' = 1.578$ $\mu$s, are separated by a free precession time $T$. (b) Mechanically driven Ramsey interferometry of the nuclear spin. The electron spin is initialized in $|\uparrow\rangle$ ($|\downarrow\rangle$) after the first $\pi/2$ nuclear rotation, corresponding to the red (blue) dots. The nuclear spin precesses at different rates depending on the state of the electron spin. The solid curves are sinusoidal fits, whose frequencies are consistent with the hyperfine coupling parameters determined earlier. (c) Ramsey oscillations measured at longer precession times. There is no decrease in the amplitude of the oscillations, indicating $T_2^* \gg 2$ ms for the $^{13}$C nuclear spin. (d) Sequence for nuclear spin echo. The $\pi$ rotation of the nuclear spin is implemented using an XY8 sequence with $2N' = 16$ and $\tau' = 1.578$ $\mu$s. (e) Spin-echo measurement showing no decay up to 10 ms, indicating $T_2^{\text{echo}} \gg 10$ ms for the $^{13}$C nuclear spin.

## III. CONCLUSION

To conclude, we coherently control a single nuclear spin with surface acoustic waves, using a SiV center as an interface, and show that the nuclear spin retains its excellent coherence properties. The power required for this approach is 2–3 orders of magnitude lower than that for other techniques [1,2,9,13,14,27,34]. This is particularly important when operating at cryogenic temperatures at which cooling power is limited, and it is therefore crucial for scaling up to more complex control sequences, as well as multiple spins and control channels. This technique can be applied to control other nuclear and electronic spins implanted into diamond and coupled to the SiV spin. This approach can also be extended to platforms other than diamond, if an electronic spin with strain susceptibility comparable to that of the SiV can be found. Future developments for this work include integration with photonic structures such as tapered waveguides, which will increase the photon collection efficiency and enable single-shot spin readout [30]. Integration with phononic waveguides [22–26] will enable the routing of multiple acoustic control signals on chip and the control of multiple spins with low cross-talk. Therefore, these results open a path towards the integration of multiple, optically addressable spins and long-lived quantum memories in a scalable way, using surface acoustic waves for control.

Additionally, using a SiV with a resident $^{29}$Si nuclear spin enables the resolution of hyperfine energy levels [35], which could be used to achieve entanglement between the SiV and the nuclear spin with a single $\pi$ pulse. At the same time, strong coupling between the SiV spin and a single phonon could be achieved using a high-quality-factor, low-mode-volume mechanical resonator [31,36,37], thus enabling single-phonon spin gates. This would enable the use of single nuclear spins as quantum memories for phononic states, with potential applications in metrology, quantum sensing [38], quantum information processing [16,39–42], and fundamental tests of quantum theory [43–45].

The data shown in the figures is available in Ref. [46].

## APPENDIX A: DEVICE FABRICATION

We use [100]-cut, electronic-grade, single-crystal diamond samples synthesized by chemical vapor deposition (CVD) from Element Six Corporation. Silicon ions ($^{28}Si^+$) are implanted on the top surface of the diamond at an energy of 150 keV and a density of $10^{10}$ cm$^{-2}$, introducing Si atoms over the entire surface at a depth of $100 \pm 18$ nm as determined by a SRIM simulation [47]. SiV centers are generated by a high-temperature (1200 °C), high-vacuum annealing procedure followed by a tri-acid cleaning (1 : 1 : 1 sulphuric, perchloric, and nitric acids). A 1.4-$\mu$m aluminium nitride (AlN) layer is deposited on top of the diamond by rf sputtering. IDTs are fabricated using electron beam lithography followed by evaporation of 75 nm of aluminium (Al). The SAWs propagate along the [110] direction, parallel to one of the edges of the sample. Further details on the design and characterization of IDTs may be found in Ref. [29].

## APPENDIX B: EXPERIMENTAL SETUP

Low-temperature measurements are performed in a $^3$He/$^4$He dilution refrigerator (Bluefors LD250) with a base temperature of 10 mK. The diamond sample is mounted on a plate that is thermally anchored to the mixing plate of the refrigerator. The diamond is affixed with indium foil to a custom-made holder made of copper, which is located on top of an XY nanopositioner stack. IDTs on the sample are wire bonded to a printed circuit board (PCB) mounted on the holder for electrical excitation of acoustic pulses. A thermometer located close to the sample indicates a typical temperature of 50–200 mK during our experiments. The sample is surrounded by a three-axis superconducting vector magnet system used to apply a static magnetic field. Above the sample, a cryogenic objective (attocube LT-APO/VISIR/0.82) with a numerical aperture of 0.82 and a working distance of 0.65 mm is mounted on a Z nanopositioner. A homemade confocal microscope is used for optical excitation and fluorescence collection. A tunable laser stabilized to an accuracy of 0.01 pm using feedback from a wavelength meter is used to resonantly excite optical transitions of individual SiVs. Photons emitted by individual SiVs in the phonon sideband (PSB) greater than 740 nm are selected by an optical long-pass filter and sent to an avalanche photodiode (APD).

## APPENDIX C: GENERATION OF OPTICAL AND ACOUSTIC PULSES

Laser pulses at 737 nm are generated using an acousto-optic modulator (AOM). The AOM is driven by a custom-built rf driver and is used in a double-pass configuration to achieve an extinction ratio greater than 70 dB, which is required to prevent unwanted optical spin pumping during long experimental sequences. A time-correlated single photon counter (TCSPC) is used to record arrival times of photons emitted from the SiV. An arbitrary waveform generator (AWG) controls the entire experimental sequence. The 8-bit analog output of the AWG is used to drive the IDTs, while the two 1-bit marker outputs are used to control the AOM and trigger the TCSPC. There is a small amount of drift between the clocks of the AWG and TCSPC, with a factor of about $1.25 \times 10^{-5}$, for which we correct in our data processing.

## APPENDIX D: SiV SPIN INITIALIZATION

The SiV can be initialized in $|\uparrow\rangle$ or $|\downarrow\rangle$ by resonantly pumping the optical transitions $\downarrow\downarrow'$ or $\uparrow\uparrow'$, respectively. For our experiments, after the acoustic $\pi$ pulse is calibrated, we initialize the SiV in $|\uparrow\rangle$ by optically pumping $\downarrow\downarrow'$, and in $|\downarrow\rangle$, by optically pumping $\downarrow\downarrow'$ followed by an acoustic $\pi$ pulse. This allows us to keep the wavelength of the laser resonant with the $\downarrow\downarrow'$ transition. We insert an acoustic $\pi$ pulse between the final optical readout pulse of one experimental sequence and the optical initialization pulse of the next sequence so that the SiV is in $|\downarrow\rangle$ before the initialization pulse. This allows the photon counts during the initialization pulse to be used as a measure of the population in $|\downarrow\rangle$.

## APPENDIX E: SiV SPIN POPULATION MEASUREMENT

The arrival times of photons emitted by the SiV are accumulated in a histogram over multiple ($10^6 - 10^8$) repetitions of the experimental sequence. The fluorescence photon counts are integrated for the first 100 ns of optical pumping [34]. The spin population of the SiV is measured as the ratio of the integrated fluorescence during the optical readout pulse to that during the optical initialization pulse. The spin projection of the SiV is calculated as $\langle \sigma_z \rangle = 1 - 2P_\downarrow$, in which $P_\downarrow$ is the population in the $|\downarrow\rangle$ state.

## APPENDIX F: NUCLEAR SPIN ROTATIONS

For the value of $\tau = 1.569\ \mu$s used for nuclear initialization and readout, the rotation angle is calculated to be $\phi = 0.62\pi$, with the conditional rotation axes being $\mathbf{n}_\uparrow = (0.77, 0, 0.64)$ and $\mathbf{n}_\downarrow = (-0.69, 0, 0.72)$.

The $X$ rotations of the nuclear spin during the Rabi and Ramsey interferometry sequences are actually conditional rotations of the form $\mathcal{R}^\phi_{-\mathbf{x},\mathbf{x}}$ for the interpulse time $\tau' = 1.578\ \mu$s. However, since the electron spin is initialized in $|\uparrow\rangle$ at the end of the initialization sequence, the nuclear spin only rotates about the $+X$ axis.

[1] J. T. Muhonen, J. P. Dehollain, A. Laucht, F. E. Hudson, R. Kalra, T. Sekiguchi, K. M. Itoh, D. N. Jamieson, J. C. McCallum, A. S. Dzurak, and A. Morello, *Storing Quantum Information for 30 Seconds in a Nanoelectronic Device*, Nat. Nanotechnol. **9**, 986 (2014).

[2] C. E. Bradley, J. Randall, M. H. Abobeih, R. C. Berrevoets, M. J. Degen, M. A. Bakker, M. Markham, D. J. Twitchen, and T. H. Taminiau, *A Ten-Qubit Solid-State Spin Register with Quantum Memory up to One Minute*, Phys. Rev. X **9**, 031045 (2019).

[3] H. P. Bartling, M. H. Abobeih, B. Pingault, M. J. Degen, S. J. H. Loenen, C. E. Bradley, J. Randall, M. Markham, D. J. Twitchen, and T. H. Taminiau, *Entanglement of Spin-Pair Qubits with Intrinsic Dephasing Times Exceeding a Minute*, Phys. Rev. X **12**, 011048 (2022).

[4] T. H. Taminiau, J. Cramer, T. van der Sar, V. V. Dobrovitski, and R. Hanson, *Universal Control and Error Correction in Multi-Qubit Spin Registers in Diamond*, Nat. Nanotechnol. **9**, 171 (2014).

[5] W. Pfaff, B. J. Hensen, H. Bernien, S. B. van Dam, M. S. Blok, T. H. Taminiau, M. J. Tiggelman, R. N. Schouten, M. Markham, D. J. Twitchen, and R. Hanson, *Unconditional Quantum Teleportation between Distant Solid-State Quantum Bits*, Science **345**, 532 (2014).

[6] N. Kalb, A. A. Reiserer, P. C. Humphreys, J. J. W. Bakermans, S. J. Kamerling, N. H. Nickerson, S. C. Benjamin, D. J. Twitchen, M. Markham, and R. Hanson, *Entanglement Distillation between Solid-State Quantum Network Nodes*, Science **356**, 928 (2017).

[7] M. Pompili, S. L. N. Hermans, S. Baier, H. K. C. Beukers, P. C. Humphreys, R. N. Schouten, R. F. L. Vermeulen, M. J. Tiggelman, L. dos Santos Martins, B. Dirkse, S. Wehner, and R. Hanson, *Realization of a Multinode Quantum Network of Remote Solid-State Qubits*, Science **372**, 259 (2021).

[8] L. Jiang, J. S. Hodges, J. R. Maze, P. Maurer, J. M. Taylor, D. G. Cory, P. R. Hemmer, R. L. Walsworth, A. Yacoby, A. S. Zibrov, and M. D. Lukin, *Repetitive Readout of a Single Electronic Spin via Quantum Logic with Nuclear Spin Ancillae*, Science **326**, 267 (2009).

[9] J. J. Pla, K. Y. Tan, J. P. Dehollain, W. H. Lim, J. J. L. Morton, F. A. Zwanenburg, D. N. Jamieson, A. S. Dzurak, and A. Morello, *High-Fidelity Readout and Control of a Nuclear Spin Qubit in Silicon*, Nature (London) **496**, 334 (2013).

[10] M. H. Metsch, K. Senkalla, B. Tratzmiller, J. Scheuer, M. Kern, J. Achard, A. Tallaire, M. B. Plenio, P. Siyushev, and F. Jelezko, *Initialization and Readout of Nuclear Spins via a Negatively Charged Silicon-Vacancy Center in Diamond*, Phys. Rev. Lett. **122**, 190503 (2019).

[11] A. Laucht, J. T. Muhonen, F. A. Mohiyaddin, R. Kalra, J. P. Dehollain, S. Freer, F. E. Hudson, M. Veldhorst, R. Rahman, G. Klimeck, K. M. Itoh, D. N. Jamieson, J. C. McCallum, A. S. Dzurak, and A. Morello, *Electrically Controlling Single-Spin Qubits in a Continuous Microwave Field*, Sci. Adv. **1**, e1500022 (2015).

[12] C. T. Nguyen, D. D. Sukachev, M. K. Bhaskar, B. Machielse, D. S. Levonian, E. N. Knall, P. Stroganov, R. Riedinger, H. Park, M. Lončar, and M. D. Lukin, *Quantum Network Nodes Based on Diamond Qubits with an Efficient Nanophotonic Interface*, Phys. Rev. Lett. **123**, 183602 (2019).

[13] A. J. Sigillito, A. M. Tyryshkin, T. Schenkel, A. A. Houck, and S. A. Lyon, *All-Electric Control of Donor Nuclear Spin Qubits in Silicon*, Nat. Nanotechnol. **12**, 958 (2017).

[14] S. Asaad, V. Mourik, B. Joecker, M. A. I. Johnson, A. D. Baczewski, H. R. Firgau, M. T. Mądzik, V. Schmitt, J. J. Pla, F. E. Hudson, K. M. Itoh, J. C. McCallum, A. S. Dzurak, A. Laucht, and A. Morello, *Coherent Electrical Control of a Single High-Spin Nucleus in Silicon*, Nature (London) **579**, 205 (2020).

[15] S. Thiele, F. Balestro, R. Ballou, S. Klyatskaya, M. Ruben, and W. Wernsdorfer, *Electrically Driven Nuclear Spin Resonance in Single-Molecule Magnets*, Science **344**, 1135 (2014).

[16] M. J. A. Schuetz, E. M. Kessler, G. Giedke, L. M. K. Vandersypen, M. D. Lukin, and J. I. Cirac, *Universal Quantum Transducers Based on Surface Acoustic Waves*, Phys. Rev. X **5**, 031031 (2015).

[17] P. Delsing *et al.*, *The 2019 Surface Acoustic Waves Roadmap*, J. Phys. D **52**, 353001 (2019).

[18] M. Mirhosseini, A. Sipahigil, M. Kalaee, and O. Painter, *Superconducting Qubit to Optical Photon Transduction*, Nature (London) **588**, 599 (2020).

[19] R. K. Sundfors, *Nuclear Acoustic Resonance of* $^{73}$Ge *in Single-Crystal Germanium; Interpretation of Experimental Gradient-Elastic-Tensor Components in Germanium and Zinc-Blende Compounds*, Phys. Rev. B **20**, 3562 (1979).

[20] Y. Okazaki, I. Mahboob, K. Onomitsu, S. Sasaki, S. Nakamura, N.-H. Kaneko, and H. Yamaguchi, *Dynamical Coupling between a Nuclear Spin Ensemble and Electromechanical Phonons*, Nat. Commun. **9**, 2993 (2018).

[21] L. A. O'Neill, B. Joecker, A. D. Baczewski, and A. Morello, *Engineering Local Strain for Single-Atom Nuclear Acoustic Resonance in Silicon*, Appl. Phys. Lett. **119**, 174001 (2021).

[22] D. Hatanaka, I. Mahboob, K. Onomitsu, and H. Yamaguchi, *Phonon Waveguides for Electromechanical Circuits*, Nat. Nanotechnol. **9**, 520 (2014).

[23] K. Fang, M. H. Matheny, X. Luan, and O. Painter, *Optical Transduction and Routing of Microwave Phonons in Cavity-Optomechanical Circuits*, Nat. Photonics **10**, 489 (2016).

[24] W. Fu, Z. Shen, Y. Xu, C.-L. Zou, R. Cheng, X. Han, and H. X. Tang, *Phononic Integrated Circuitry and Spin–Orbit Interaction of Phonons*, Nat. Commun. **10**, 2743 (2019).

[25] F. M. Mayor, W. Jiang, C. J. Sarabalis, T. P. McKenna, J. D. Witmer, and A. H. Safavi-Naeini, *Gigahertz Phononic Integrated Circuits on Thin-Film Lithium Niobate on Sapphire*, Phys. Rev. Applied **15,** 014039 (2021).

[26] L. Shao, D. Zhu, M. Colangelo, D. H. Lee, N. Sinclair, Y. Hu, P. T. Rakich, K. Lai, K. K. Berggren, and M. Loncar, *Electrical Control of Surface Acoustic Waves*, arXiv: 2101.01626.

[27] C. T. Nguyen, D. D. Sukachev, M. K. Bhaskar, B. Machielse, D. S. Levonian, E. N. Knall, P. Stroganov, C. Chia, M. J. Burek, R. Riedinger, H. Park, M. Lončar, and M. D. Lukin, *An Integrated Nanophotonic Quantum Register Based on Silicon-Vacancy Spins in Diamond*, Phys. Rev. B **100,** 165428 (2019).

[28] S. Kono, K. Koshino, D. Lachance-Quirion, A. F. van Loo, Y. Tabuchi, A. Noguchi, and Y. Nakamura, *Breaking the Trade-off between Fast Control and Long Lifetime of a Superconducting Qubit*, Nat. Commun. **11,** 3683 (2020).

[29] S. Maity, L. Shao, S. Bogdanović, S. Meesala, Y.-I. Sohn, N. Sinclair, B. Pingault, M. Chalupnik, C. Chia, L. Zheng, K. Lai, and M. Lončar, *Coherent Acoustic Control of a Single Silicon Vacancy Spin in Diamond*, Nat. Commun. **11,** 193 (2020).

[30] D. D. Sukachev, A. Sipahigil, C. T. Nguyen, M. K. Bhaskar, R. E. Evans, F. Jelezko, and M. D. Lukin, *Silicon-Vacancy Spin Qubit in Diamond: A Quantum Memory Exceeding 10 ms with Single-Shot State Readout*, Phys. Rev. Lett. **119,** 223602 (2017).

[31] S. Meesala, Y.-I. Sohn, B. Pingault, L. Shao, H. A. Atikian, J. Holzgrafe, M. Gündoğan, C. Stavrakas, A. Sipahigil, C. Chia, R. Evans, M. J. Burek, M. Zhang, L. Wu, J. L. Pacheco, J. Abraham, E. Bielejec, M. D. Lukin, M. Atatüre, and M. Lončar, *Strain Engineering of the Silicon-Vacancy Center in Diamond*, Phys. Rev. B **97,** 205444 (2018).

[32] T. H. Taminiau, J. J. T. Wagenaar, T. van der Sar, F. Jelezko, V. V. Dobrovitski, and R. Hanson, *Detection and Control of Individual Nuclear Spins Using a Weakly Coupled Electron Spin*, Phys. Rev. Lett. **109,** 137602 (2012).

[33] M. A. Ali Ahmed, G. A. Álvarez, and D. Suter, *Robustness of Dynamical Decoupling Sequences*, Phys. Rev. A **87,** 042309 (2013).

[34] See Supplemental Material at http://link.aps.org/supplemental/10.1103/PhysRevX.12.011056 for additional details and results.

[35] B. Pingault, D.-D. Jarausch, C. Hepp, L. Klintberg, J. N. Becker, M. Markham, C. Becher, and M. Atatüre, *Coherent Control of the Silicon-Vacancy Spin in Diamond*, Nat. Commun. **8,** 15579 (2017).

[36] M. J. Burek, J. D. Cohen, S. M. Meenehan, N. El-Sawah, C. Chia, T. Ruelle, S. Meesala, J. Rochman, H. A. Atikian, M. Markham, D. J. Twitchen, M. D. Lukin, O. Painter, and M. Lončar, *Diamond Optomechanical Crystals*, Optica **3,** 1404 (2016).

[37] L. Shao, S. Maity, L. Zheng, L. Wu, A. Shams-Ansari, Y.-I. Sohn, E. Puma, M. Gadalla, M. Zhang, C. Wang, E. Hu, K. Lai, and M. Lončar, *Phononic Band Structure Engineering for High-Q Gigahertz Surface Acoustic Wave Resonators on Lithium Niobate*, Phys. Rev. Applied **12,** 014022 (2019).

[38] C. L. Degen, F. Reinhard, and P. Cappellaro, *Quantum Sensing*, Rev. Mod. Phys. **89,** 035002 (2017).

[39] T. A. Palomaki, J. W. Harlow, J. D. Teufel, R. W. Simmonds, and K. W. Lehnert, *Coherent State Transfer between Itinerant Microwave Fields and a Mechanical Oscillator*, Nature (London) **495,** 210 (2013).

[40] Y. Chu, P. Kharel, W. H. Renninger, L. D. Burkhart, L. Frunzio, P. T. Rakich, and R. J. Schoelkopf, *Quantum Acoustics with Superconducting Qubits*, Science **358,** 199 (2017).

[41] P. Arrangoiz-Arriola, E. A. Wollack, M. Pechal, J. D. Witmer, J. T. Hill, and A. H. Safavi-Naeini, *Coupling a Superconducting Quantum Circuit to a Phononic Crystal Defect Cavity*, Phys. Rev. X **8,** 031007 (2018).

[42] K. J. Satzinger, Y. P. Zhong, H.-S. Chang, G. A. Peairs, A. Bienfait, M.-H. Chou, A. Y. Cleland, C. R. Conner, É. Dumur, J. Grebel, I. Gutierrez, B. H. November, R. G. Povey, S. J. Whiteley, D. D. Awschalom, D. I. Schuster, and A. N. Cleland, *Quantum Control of Surface Acoustic-Wave Phonons*, Nature (London) **563,** 661 (2018).

[43] M. Berta, M. Christandl, R. Colbeck, J. M. Renes, and R. Renner, *The Uncertainty Principle in the Presence of Quantum Memory*, Nat. Phys. **6,** 659 (2010).

[44] A. Bassi, K. Lochan, S. Satin, T. P. Singh, and H. Ulbricht, *Models of Wave-Function Collapse, Underlying Theories, and Experimental Tests*, Rev. Mod. Phys. **85,** 471 (2013).

[45] M. Aspelmeyer, T. J. Kippenberg, and F. Marquardt, *Cavity Optomechanics*, Rev. Mod. Phys. **86,** 1391 (2014).

[46] S. Maity, B. Pingault, G. Joe, M. Chalupnik, D. Assumpção, E. Cornell, L. Shao, and M. Lončar, *Mechanical Control of a Single Nuclear Spin*, 2020, 10.5281/zenodo.6374506.

[47] J. F. Ziegler, M. Ziegler, and J. Biersack, *SRIM—The Stopping and Range of Ions in Matter*, Nucl. Instrum. Methods Phys. Res., Sect. B **268,** 1818 (2010).